Unsteady flow structures in the tip region for a centrifugal compressor impeller before rotating stall

ZHAO HuiJing, WANG ZhiHeng & XI Guang*

School of Energy and Power Engineering, Xi'an Jiaotong University, Xi'an 710049, China

To get an insight into the occurrence and the mechanism of flow unsteadiness in the tip region of centrifugal compressor impellers, the flow in Krain's impeller is investigated by using both steady and unsteady RANS solver techniques. It is found that the flow unsteadiness on the pressure side is much stronger than that on the suction side. The periodical frequency of the unsteady flow is around half of the blade passing frequency. The originating mechanism of the flow unsteadiness is illustrated with the time-dependent tip leakage flow and blade loading at the tip region. Due to the blockage caused by the joint effects of broken-downed tip leakage vortex, separated fluids and tip leakage flow at downstream, a low pressure region is formed on the pressure side, consequently the blade loadings is altered. In turn, the changed blade loadings will alter the intensity of tip leakage flow. Such alternative behavior finally results in the periodic process. By comparing the calculated flow field in the cases of single-passage and four-passage models, it is confirmed that the investigated flow unsteadiness is confined in each single passage, as no phase differences are found in the model of four passages. This is different from the situation in axial compressor when the rotating instability is encountered. The flow unsteadiness only occurs at the working conditions with small mass flow rates, and the oscillation intensity will be enhanced with the decrease of mass flow rate. When the mass flow rate is too small, the flow unsteadiness in a single passage may trigger rotating stall, as the disturbance propagates in the circumferential direction.

centrifugal compressor impeller, flow unsteadiness, tip leakage flow, blade loading

1 Introduction

In dynamic compressors, the unstable phenomena known as rotating stall and surge, induce a considerable drop of performance in terms of pressure ratio, efficiency, and structural integrity. Consequently, extending the stable operating range has been the pursuit of compressor researchers. The flow structures in the tip region were found to have a significant effect on the flow stability of compressors by the existing experimental and numerical studies [1–3]. The control measures, such as tip injection and casing treatments, could de-crease the low-energy fluid in the tip region, and thus they were effective to extend the compressor stall margin [4–6]. To further expand the stable operating range, the deep understanding of the flow structures arising prior to the stall onset is required. Therefore, the flow structures in the tip region have drawn much of attentions of the researchers in turbomachinery aerodynamics.

As for axial compressors, there are two kinds of transient flow patterns as reported in open literatures. Both of them are highly correlated with the tip leakage flow (TLF). One transient flow pattern is the self-induced unsteadiness of tip leakage vortex (TLV) confined in a single passage. Du et al. [7,8] investigated the flow structures in the tip region for dif-

ferent axial transonic rotors by numerical simulations and experiments. The results showed that, at the near-stall point, the TLF impinged on the pressure side of adjacent blade, creating low pressure spots on the pressure side and variation in the near-tip blade loading, which was thought to originate the self-induced unsteadiness. Through the five-passage numerical simulation, they indicated that there existed negligible phase difference among the five passages. Meanwhile, Wu et al. [9,10] proposed another mechanism for the self-induced unsteadiness. They stated that the interaction between the broken-down TLV and the TLF from adjacent passages formed a tip separation vortex. The cyclic motion of tip separation vortex established a self-sustained unsteadiness in tip flow fields. To be noted, the whole-passage simulation showed the tip separation vortice was confined in each passage, no periodical variation was observed across passages. The other unsteady flow pattern is the rotating instability in multiple passages or the full annulus. The periodical interaction between the TLF of one blade and the flow at the adjacent blade lead to the strong oscillation of blade tip vortex. The fluctuating blade tip vortex would propagate in the circumferential direction along the rotor blade row, and thus the rotating instability was triggered [11].

However, there is limited information in literatures on the unsteady behavior and mechanism of the TLF for centrifugal compressors. Yang et al. [12] conducted an unsteady simulation at the stall onset. The static pressure at 90% span showed significant unsteadiness due to the TLF/mainflow interaction. Because of the periodical interaction between the TLV and the mainflow, the vorticity of TLV varied with time, and the vortex shed periodically. However, the unsteady flow before the stall onset was not analyzed in their work, and it was still not clear whether the flow unsteadiness occured before the stall onset. In the experimental study of Schleer et al. [13], they indicated that a region with high pressure unsteadiness originated at the leading edge of the main blade, it propagated downstream before the rotating stall was initiated. The unsteady area was overlapped with the TLV trajectory. Bousquet et al. [14] conducted a 3D unsteady simulation by considering both impeller and vaned diffuser of full annulus. They found that the shear stress layer at the interface between the mainflow and low-moment fluid area became unstable at near-stall conditions. A periodical vortex shedding was observed. Such unsteady phenomenon was also called Kelvin-Helmholtz instability. To sum up, the flow unsteadiness appears in the tip region of centrifugal compressors before the rotating stall onset, it may be used as an indicator to predict the rotating stall.

Much effort was also made to explore the possible link between the TLF and the stall inception process. Hoying et al. [15] simulated the spike rotating stall inception for the low-speed E3 compressor. They found that the stall inception was a result of tip clearance vortex moving upstream of the blade passage. When the vortex trajectory was aligned with the blade leading edge plane, the spike stall appeared. Vo et al. [16] proposed two conditions necessary for the formation of spike stall: one was that the spillage of TLF to the adjacent blade passage ahead of the rotor leading edge and below the blade tip, and the other was the initiation of backflow stemming from the leakage fluid in adjacent passages at the trailing edge plane. Furthermore, Chen et al. [17] carried out the full-annulus calculations to study the pre-stall behavior of a transonic axial compressor. They indicated that the rotating stall developed from the growth of rotating instabilities, and a rotating long-length disturbance was followed by a spike-type breakdown. Concerning about the TLV development with the decrease of mass flow rate in axial compressors, three modes were proposed by Tong et al. [18]. They were steady mode, in-blade unsteady mode (so called self-induced unsteadiness) and cross-blade unsteady mode (so called spike stall). Tong et al. [18] stated that the precursor of a spike stall was originated from the circumferential location where the strongest in-blade unsteady TLV was located. They also demonstrated that the stall margin of a low-speed compressor rotor would be extended by inhibiting the self-induced TLF unsteadiness with micro tip injection. However, the exact flow mechanism underlying the relation between TLF unsteadiness and rotating stall is not clear at the moment, which is an interesting and important research topic. In centrifugal compressors, very few researches have been reported on the relation between TLF unsteadiness and the rotating stall. Therefore, the inspiration to investigate the unsteady flow in the tip region of centrifugal compressor impellers before rotating stall is initiated.

To answer the above questions, this paper is organized as following. After a brief introduction of Krain's impeller and the computational fluid dynamics scheme, the numerical results are validated with the available experimental results. Having identified the location and frequency of the flow unsteadiness by relative standard deviation and fast Fourier transform of static pressure, we investigate the instantaneous flow fields, and clarify the mechanism of the unsteady flow at small mass flow rates by single-passage simulation. The flow unsteadiness is further verified to be confined to each single passage without rotation from one passage to the other by the four-passage simulation. For the features of variable operating points, the unsteady strength enhances and the frequency decreases slightly as the mass flow rate decreases, and when the mass flow rate is small enough, a lower frequency appears.

2 Computational model and method

2.1 Numerical model

The transonic centrifugal compressor impeller designed by Krain et al. [19] is chosen as the research object of this pa-

per. Its complete test data and geometry parameters are open and available, so the impeller is intensively studied by many researchers [20,21]. Table 1 lists the main technical parameters of the impeller. More details of the impeller can refer to ref. [20]. The design rotational speed is 50000 r/min. To avoid inlet shockwaves, the flow analysis is carried out at the condition that the impeller runs at 70% design speed.

2.2   Mesh parameters

In this study, both the models with single passage and four passages are used. The computational domain consists of the impeller, the intake passage upstream and the vaneless diffuser downstream. The ANSYS TURBOGRID is used to generate the computational grid, and an automatic topology is used for the blade passage. The topology type enables us to create high-quality meshes (in terms of edge length ratio, orthogonality and aspect ratio) with acceptable nodes. The computational domain and mesh distributions near the leading edge (LE) and trailing edge (TE) are shown in Figure 1. To ensure the computational independence of grid distribution, the grid independence study is conducted with four sets of meshes: 3.4×10^5, 6.2×10^5, 9.2×10^5, 1.2×10^6. It is proved that the mesh with 9.2×10^5 nodes is sufficient for the computation, which achieves a well balance between accuracy and computational cost. The mesh distribution is $150\times50\times73$ in streamwise, blade-to-blade and spanwise directions, respectively. Eighteen nodes are used in the tip clearance. The size of the first cell is set to be 8 μm, which corresponds to $y+<5$ at the walls. For the four-passage model, the grid is transformed

Table 1   Design specifications of impeller

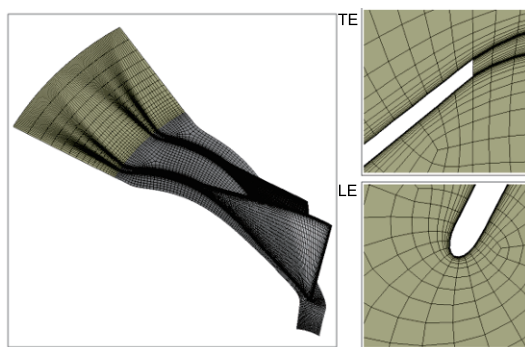| Design parameters	Value
Design mass flow (kg/s)	2.55
Inlet tip diameter (mm)	156
Inlet hub diameter (mm)	60
Impeller diameter (mm)	224
Impeller outlet width (mm)	10.2
Blade number	13/13

Figure 1   (Color online) Computational mesh.

by turbo rotation, and the number of nodes is 3.68×10^6 in total.

2.3   Flow solver and numerical parameters

To analyze the flow structures in the tip region, the 3D unsteady and steady, Reynolds Averaged Navier-Stokes (RANS) equation and shear stress transport (SST) turbulent model are solved with ANSYS CFX 13.0, which was demonstrated to can well predict the flow in the tip region by the work of Decaix et al. [22], Roberts and Steed [23] in an airfoil with different tip clearances. A second order accurate total variation diminishing scheme is used to evaluate the advection term. The viscous term is determined in a central difference manner. For the unsteady numerical simulation, the transient term is performed with an implicit time-step scheme, which is composed of the second order backward Euler scheme. The time step independence study is conducted by three sets of time steps: 30, 60, 90 per main blade passage. It shows that the number of time steps has almost no effects on the flow structures and frequency characteristics. To achieve the accurate results with minimum cost, the number of time steps to discretize the main blade-passing period is set to 60. For each time step, 10 inner iterations are used. At least 15 impeller rotations are needed to reach the periodic state, which corresponds to approximately 12000 time steps.

2.4   Boundary conditions

To be consistent with the experimental data provided in ref. [20], the total pressure, total temperature and flow direction are given at the inlet of impeller. At the vaneless diffuser exit, the static pressure or mass flow rate is specified. Meanwhile, nonslip and adiabatic conditions are imposed on all the solid walls. The circumferential sides of the computational domain are set as rotational periodicity boundary. For the steady numerical simulation, the converged results are obtained when the following criteria are satisfied: (1) the RMS residuals fall below 1.0×10^{-5}; (2) the value difference in mass flow rates between inlet and outlet of the computational domain is less than 0.1%; (3) the variation of efficiency is less than 0.01%; (4) the imbalances of momentum equation, conservation equation and energy equation are less than 0.01%. The steady simulation results are then used as initial conditions for the unsteady simulation. Several monitors are set in the impeller to monitor the periodic state.

2.5   Validation of the numerical model

In the open literatures, the experimental total pressure ratio is only obtained at 70% design speed. The comparison of total pressure ratios between experiment and numerical simulation with single-passage model is presented in Figure 2. Both steady and unsteady simulations cannot predict the stall point accurately. However, this work focuses on the unsteady
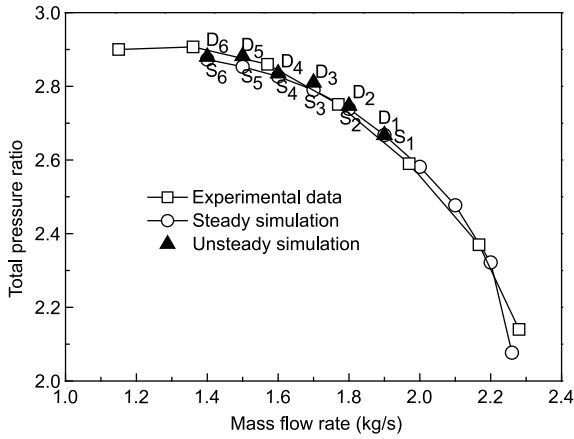
Figure 2 Comparison of calculated and experimental total pressure ratios at 70% design speed.

flow near the stall, but not on the stall, so only the operating points before the experimental surge line have been presented. The numerical investigation indicates that the flow unsteadiness cannot be predicted when the mass flow rate is larger than that at D_1. Therefore, unsteady simulation is only conducted on six operating points, which are labeled as D_1, D_2, D_3, D_4, D_5 and D_6. Correspondingly, the steady simulation is labeled as S_1, S_2, S_3, S_4, S_5 and S_6. The values and the trends of total pressure ratios predicted by steady and unsteady (time-averaged) simulations agree well with the experimental results. In the authors' previous paper [24], the numerical simulation on the Krain's impeller was conducted at design speed with the same numerical method as in the present paper, and the calculated flow field agreed well with the experimental results. It is indicated that the numerical scheme in this paper can capture the overall performance and flow structures reasonably well.

3   Results

3.1   Unsteady numerical results at D_3 by single-passage model

This paper focuses on the flow structures in the tip region

before the stall is initiated. The circumferential rotating disturbances such as leading spillage of TLV, reverse flow and etc., are not considered, as they are induced by blade-to-blade interaction after the stall onset. Therefore, a single-passage model is used to investigate the unsteady flow phenomena and mechanism. In addition, the fluctuating flow field may mix with the pre-stall flow behaviors at the near-stall point D_5, which is unfavourable for observing the flow oscillation clearly. The static pressure in the tip region already fluctuates with a prominent level at D_3, which is far away from the stall condition. Therefore, D_3 is selected for the following analysis,

3.1.1   Frequency and amplitude characteristics of static pressure

To clearly show the distribution of oscillating strength and identify the locations of the high oscillating strength, Figure 3 presents the distribution of relative standard deviation of static pressure P on the pressure side (PS) and suction side (SS). The relative standard deviation of static pressure is defined as follows:

$$\sigma_{ij} = \frac{\sqrt{\dfrac{1}{N}\sum_{j=1}^{N}\left(P_{ij} - \overline{P}_i\right)^2}}{\overline{P}_i}, \tag{1}$$

where i denotes the node in the blade passage, j denotes the time index of different time steps, $\overline{P}$ denotes the averaged static pressure and N denotes the number of time steps. The high oscillating regions of static pressure are concentrated on the tip region, which corresponds to the area influenced by the TLF. For the main blade, the flow unsteadiness on the PS is much stronger than that on the SS. There are three high oscillating regions on the PS. The highest oscillating region is located near the LE, where the TLV is strongest. The second highest oscillating region is located at the middle of main blade, which is affected by the TLF from the splitter. The third highest oscillating region is near the TE due to the TLF/wake interaction. For the splitter, there is an obvious high oscillating region near the LE, since the TLF spilled from the middle-chord of main blade interacts intensely with the LE of splitter. To analyze the frequency characteristics in
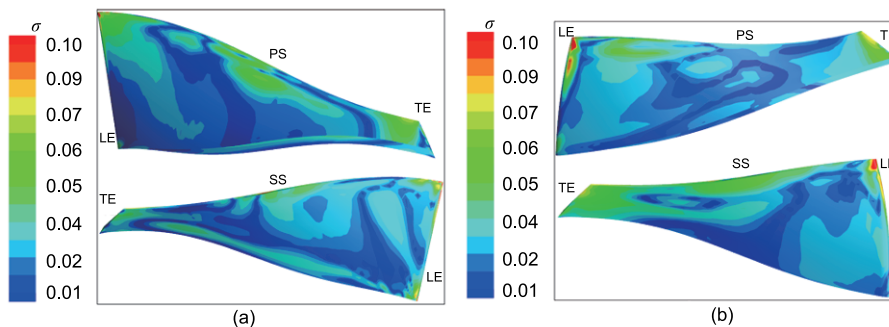

Figure 3 Relative standard deviation distribution of static pressure for blades at D_3. (a) Main blade; (b) splitter.

the relative reference frame, a total of 20 monitor points are set, and 4 of them are located at 5%, 35%, 65% and 95% span, respectively. The 4 monitors set on the PS are located at the same streamwise positions as shown in Figure 4(a). The rest 16 points are distributed on the blade-to-blade surface of 95% span as shown in Figure 4(b).

There is a main oscillation frequency component for all the monitor points. It is 3617 Hz, which corresponds to 0.477 main blade pass frequency (BPF). Figure 5(a) shows that the

oscillation at 95% span is much stronger than those at lower spanwise locations. As shown in Figure 5(b), at 95% span, the strongest oscillation is observed near the LE of main blade, and the monitor points 9 and 10 have stronger local oscillations. This matches well with the distribution of the relative standard deviation of static pressure. The result disagrees with that of Bae and Breuer [25], who found the frequency decreased gradually along the streamwise direction. However, the result agrees well with those in axial rotors [7,8].

3.1.2　*Unsteady flow characteristics*

Before the illustration of unsteady mechanism, the flow unsteadiness behaviors in the tip region are analyzed in detail by inspecting the static pressure, TLV and blade loading. Figure 6 shows the instantaneous vorticity coefficient ζ_n at five time instants within one unsteady period T. The vorticity coefficient ζ_n is defined as follows:

$$\zeta_n = \frac{|\overline{\zeta}|}{2\omega}, \tag{2}$$

where $\overline{\zeta}$ is the vorticity, and ω represents the angular velocity. The TLV trajectory can be identified by a line connecting the centers of the low pressure troughs near the shroud [26]. The

Figure 4　Monitor points distribution. (a) In the spanwise direction; (b) on the blade to blade surface of 95% span.
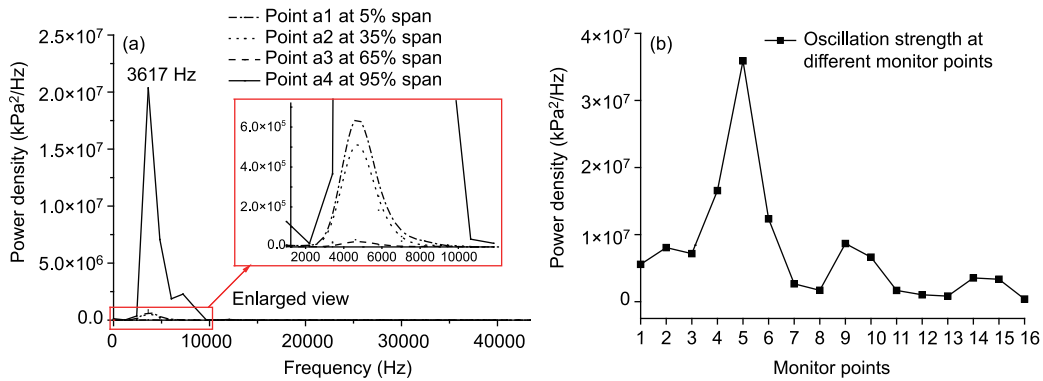

Figure 5　Frequency and amplitude characteristics in relative reference frame. (a) In spanwise direction; (b) on the blade to blade surface of 95% span.
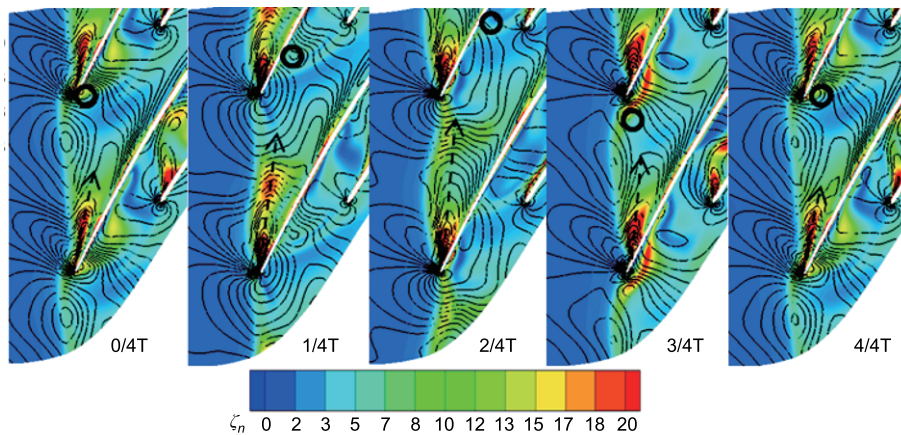

Figure 6　Instantaneous vorticity coefficient and static pressure distributions on the 95% span during one unsteady period T. The black lines, which are superimposed at each instant, represent the static pressure contours, and they are used to identify the TLV trajectory (the black dash arrows).

TLV is observed near the LE of main blade at all instants. However, both the vortex strength and the angle α between TLV trajectory and blade mean camber line vary along the time. From 0/4T to 3/4T, the TLV becomes stronger, and the angle α increases. After 3/4T, the TLV strength and the angle α decrease. At 4/4T, the TLV strength and the angle α are similar to those at 0/4T. Thus, the periodic variation forms. The previous studies [27–29] stated that the TLF or TLV mainly depended on the blade loading, and the angle α can be defined as follows:

$$\tan\alpha = \frac{k}{\overline{V}_s}\sqrt{\left(\overline{\frac{\Delta p}{\rho}}\right)_{\text{tip}}},\tag{3}$$

where the V_s is the incoming flow velocity at the impeller inlet, ρ is density, $\overline{\Delta P}$ is the averaged blade tip loading, and k is the coefficient. In this study, the V_s and ρ vary slightly along the time. As shown in Figure 7, the α and the blade loading near the LE of main blade fluctuate synchronously, so it is indicated that the fluctuating blade loading is responsible for the oscillation of α. Recalling the static pressure contours in Figure 6, a low pressure region is observed on the PS of adjacent main blade (represented by the circle) and it moves downstream along the PS. It is the motion of low pressure region that causes the fluctuation of blade loading. In the axial rotor, the low pressure region is induced by the TLV impinging with the blade [7]. However, in the centrifugal compressor impeller, the TLV cannot reach to the PS of adjacent main blade, which can be seen by the low absolute vorticity coefficient and disappeared low pressure troughs (Figure 6). Figure 8 shows the relative Mach number distributions during one unsteady period T. There are two blockage zones (low relative Mach number zones: A1 and A2) in the inducer. A1 originates from the SS. A2 is located at the PS. From 0/4T to 4/4T, A2 propagates downstream along the PS (see the black dash line in Figure 8), and it enters into the splitter passage at 4/4T. From 0/4T to 3/4T, A1 leaves the SS, and moves along the pitchwise direction. At 4/4T (0/4T), A1 reaches to the LE of adjacent main blade, turning to A2, and then moves downstream along the PS. At the same time, a new blockage zone similar with A1 appears on the SS. Thus a new cycle starts

from this instant. The trajectory of moving blockage is similar to that of low pressure region on the PS. Therefore, we can predict that the low pressure region is closely correlated with the blockage. It is our next topics to identify how the blockage is formed. The unsteadiness mechanism would also be discussed.

3.1.3   Unsteadiness mechanism associated with the blockage

In order to identify the vortex structure quantitatively, a normalized helicity (H_n) is defined as follows:

$$H_n = \frac{\overline{\zeta}\cdot\overline{W}}{|\overline{\zeta}||\overline{W}|},\tag{4}$$

where $\overline{W}$ denotes the vector of relative velocity. $H_n = 1$ or -1 indicates the vortex core, which is characterized by strong rolling up of vortex [26]. When the vortex vector and relative velocity are in the same direction, H_n is 1. Otherwise, it is -1. The change of the sign of H_n is the requirement to indicate the breakdown of TLV. M denotes the meridional distance from the LE to the TE of main blade. "0% M" means the LE, and "100% M" means the TE. Figure 9(a) presents the TLF streamlines released from 0–15% M, which are colored by the corresponding values of H_n. The H_n of TLF streamlines is -1
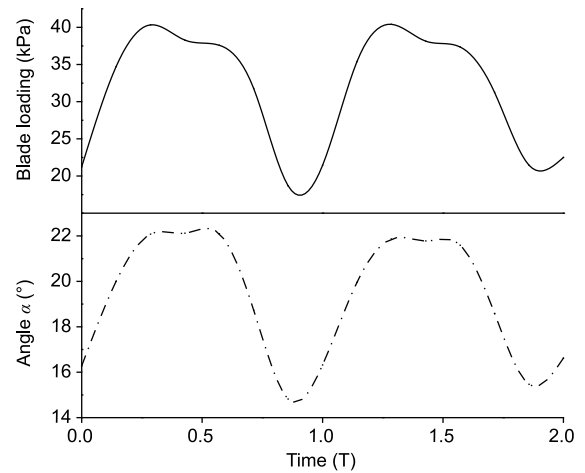
Figure 7   Blade tip loading and α variations during two unsteady period T.
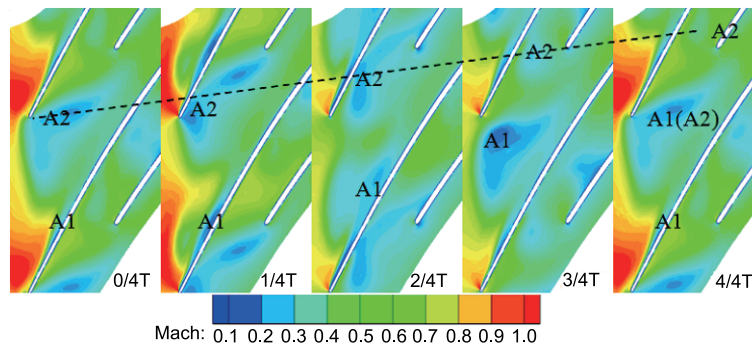
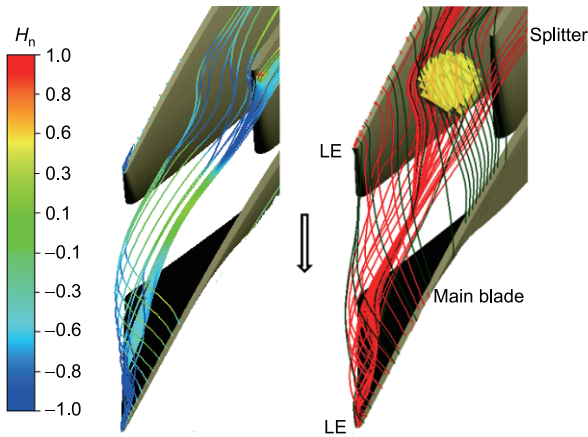**Figure 8**   Instantaneous much number distribution on 95% span during one unsteady period T.

Figure 9   The structures of TLF. (a) The TLF streamlines released from the from 0–15% *M* at 3/4T; (b) the formation of blockage at 3/4T.

Figure 10   Sketch map of interaction between broken-downed TLV and TLF from 15%–25% *M*.

near the leading edge of main blade, which indicates that the TLF streamlines are tightly wrapped. Then the value of H_n decreases gradually at downstream, and finally it becomes a positive value near the leading edge of the adjacent main blade, which indicates the breakdown of TLV. In Figure 9(b), the red lines denote the TLF streamlines in Figure 9(a) (released from 0–15% *M*), and the green lines denote the TLF streamlines released from 15%–25% *M* in the tip clearance. Thereafter, the broken-downed TLV, carrying the separated fluids from the SS interacts with the TLF released from 15%–25% *M*, and a blockage zone is formed (yellow zone in Figure 9(b)). To further illustrate the mechanism of this phenomenon, a sketch map is presented in Figure 10. The TLF streamlines from 15%–25% *M* leave the tip clearance with an angle δ against the streamwise direction, so they have a velocity component perpendicular to the streamwise direction. The broken-downed TLV is almost in the streamwise direction. These two streams interact with each other as follows: the broken-downed TLV radially moves away from the shroud and shifts toward the PS of adjacent main blade under the intrusion action of TLF from 15%–25% *M*; the TLF from 15%–25% *M* turns to the streamwise direction. Thus, the blockage is formed.

In Figure 11, the red and green TLF streamlines are released from 0–15% *M* and 15%–25% *M*, respectively, which are the same as those depicted in Figure 9. To analyze the unsteadiness of blockage, the blockage is represented with blue lines, which are confined by $W/V_2 < 0.25$ (where W is the relative velocity and V_2 is the tip speed). From 0/4T to 3/4T, the blockage moves downstream. This is consistent with the trajectory of low pressure region on PS shown in Figures 6 and 12. From 2/4T to 4/4T, a new blockage is formed, which shifts toward the LE of adjacent main blade. At 4/4T, the new blockage reaches to the LE of adjacent main blade. Correspondingly, a new low pressure region is observed. Therefore, it is verified that the blockage causes the low pressure region on the PS. However, what is the mechanism of unsteadiness? How is it
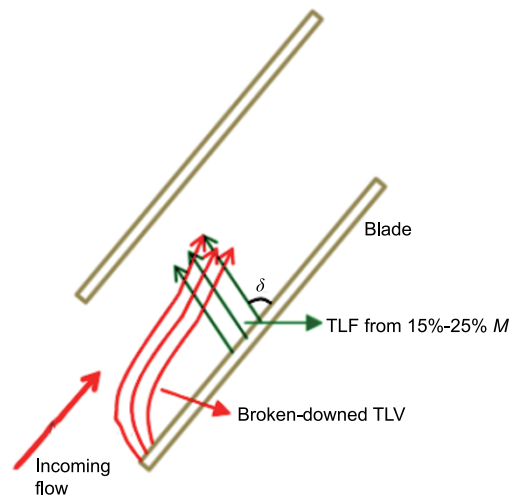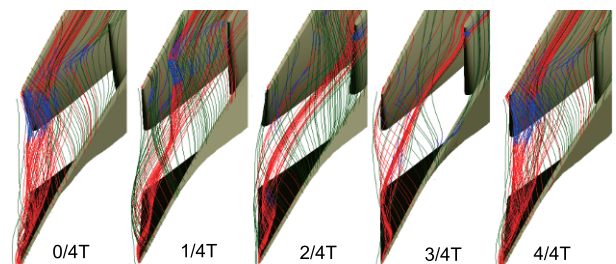

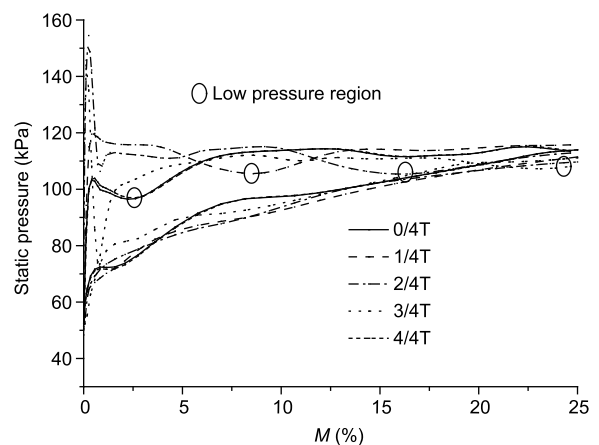**Figure 11**   Instantaneous TLF streamlines during one unsteady period T.

Figure 12   Instantaneous blade loading variations of main blade during one unsteady period T.

related to the blockage or low pressure region? They are our interest to answer these questions next.

At 0/4T, due to the high blade loading at the 15%–25% *M*, the green streamlines cause blockage at the LE of main blade, so a low pressure region is observed, which would decrease the blade loading in this area. As shown in Figure 6, the angle α is small, the TLV is weak, and the low pressure troughs are shallow. The incoming flow forms a high pressure region near

the LE of main blade. As the time proceeds, the low pressure region propagates downstream along the PS due to the push of the high pressure region. The blade loading near the LE starts to increase gradually, so the angle α becomes larger, and the TLV becomes stronger. However, the blade loading at 15%–25% M decreases due to the low pressure region, and thus the green streamlines leave the tip clearance with a smaller flow angle δ. The blockage as well as the low pressure region moves downstream further. At 3/4T, the low-pressure region reaches to 25% M, and the blade loading at 15%–25% M starts to recover. As a consequence, the green streamlines leave the tip clearance with larger flow angle δ. As shown in Figure 6, at 3/4T, a new low pressure region moves to the LE of main blade due to the upstream-moving green streamlines. Correspondingly, the blade loading near the LE and the angle α start to decrease gradually. At 4/4T, the low pressure region reaches to the same location at 0/4T. Thus a new period cycle is initiated from this point. With above discussion, we can conclude that the blockage caused by the interactions among broken-downed TLV, separated fluids and TLF from 15%–25% M contributes to the flow unsteadiness. The periodic motion of blockage leads to periodical variation of blade loading. In turn, the blade loading changes the strength of TLV and TLF, and accordingly the blockage.

To further illustrate the blade loading unsteadiness, the TLF momentum L is studied. As shown in Figure 13, the TLF momentums L from both 0–15% M and 15%–25% M vary with time periodically. However, there is a phase lag between the momentums L from 0–15% M and 15%–25% M as shown by the dash line, which is owing to the fact that the low pressure region propagates along the PS. At 6/7T, corresponds to the smallest blade loading, the momentum L from 0–15% M is the smallest, and the momentum L from 15%–25% M reaches to the lowest point at 11/7T as the low pressure region propagates.

3.2 Unsteady numerical results at D_3 by four-passage model

The analysis in Section 3.1 is conducted with the single-passage model. To prove the correctness of single-passage model and to identify whether the flow unsteadiness is correlated with rotating instability, the stimulation with four-passage model is conducted at D_3. In the four-passage simulation, a main frequency (3921 Hz) is observed in all passages, which is close to that in the single-passage computation (3617 Hz). The small difference between two frequencies (less than 10%) may be due to the numerical errors. Figure 14 shows the static pressure distributions at 95% span at two different instants. Recalling Figure 6, the flow details of the single-passage model are nearly the same as those of four-passage model (Figure 14). The centers of the low pressure troughs are connected by the dash lines to represent the TLV trajectory. The TLV trajectories in four
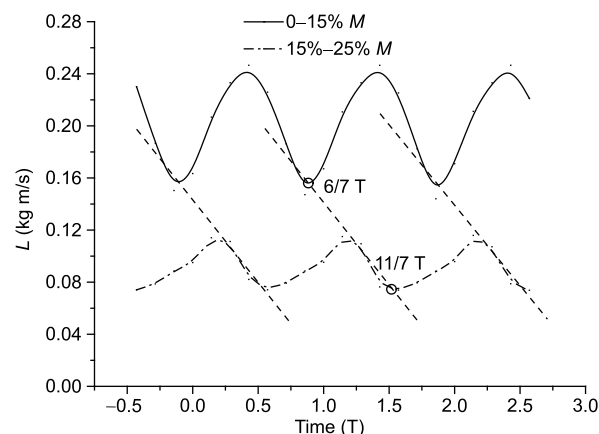

Figure 13 Time history of momentum of TLF.
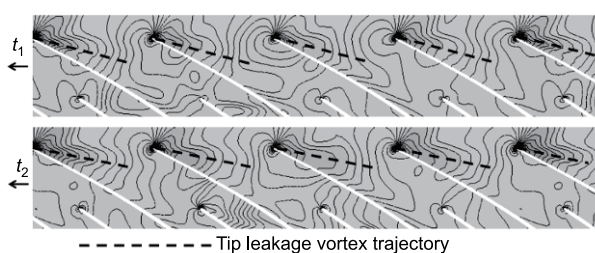

- - - - - - - - Tip leakage vortex trajectory

Figure 14 Instantaneous static pressure distributions at 95% span for the four-passage computation.

passages vary synchronously with time, and they do not reach to the PS of adjacent main blade. No phase difference is observed among the four passages at the same instant. The negligible difference of static pressure distributions among the four passages may due to the cyclic periodicity. It is indicated that the flow unsteadiness is confined to each single passage without the rotation from one passage to another, and thus it is different from the rotating instability [11,30]. Instead, the unsteady flow in the present study is similar to the "self-induced unsteadiness" in axial compressors [7–10]. It is indicated the existence of the rotation of the flow unsteadiness in the adjacent passages may depend on the special research objects. As the single-passage model is able to capture the unsteady flow structures accurately, it is used in this study to save computational time and source.

4 Discussion

4.1 Effects of mass flow rate on flow unsteadiness

It was the flow in the impeller that caused the aerodynamic instability of the present centrifugal compressor [31]. Therefore, it is of great importance to study the flow unsteadiness in the inducer at different mass flow rates

Figure 15 shows the time histories of static pressures at the same locations (see point 6 in the Figure 4(b)) of different mass flow rates. At the mass flow rate of 1.9 kg/s, the pressure
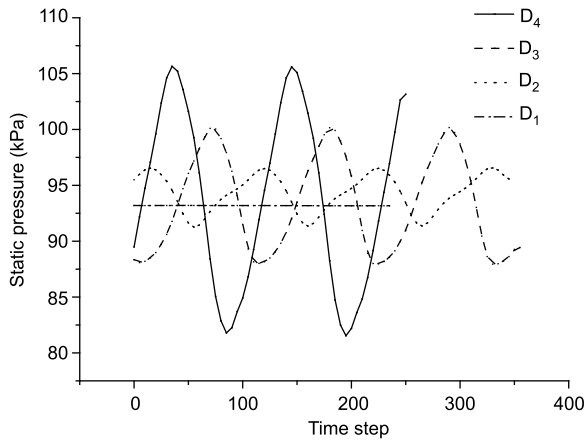
Figure 15 Fluctuation of static pressure for different operating points.

is nearly steady. As the mass flow rate decreases, the amplitude of pressure fluctuation increases, and the fluctuation amplitude at the mass flow rate of 1.6 kg/s is nearly four times of that at the mass flow rate of 1.8 kg/s. In Figure 16, the fluctuation frequency decreases slightly with the decrease of mass flow rate, which is similar to that in axial rotors. The blockage induces the flow unsteadiness, so the flow unsteadiness enhancement may be associated with the increasing blockage.

The blockage is induced by the interactions among the separated fluids, broken-downed TLV and TLF from 15%–25% M in the inducer. First of all, the TLF features at different mass flow rates are analyzed. Recalling Figure 2, the performance calculated by steady solver agrees well with the time-
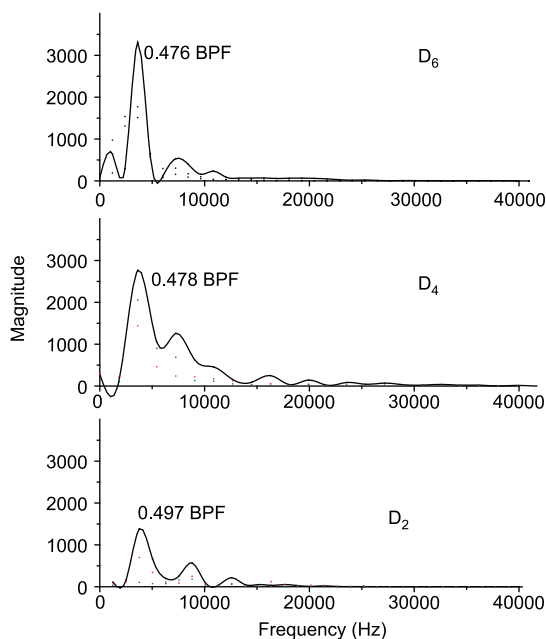
averaged one and experiment, so a steady simulation is conducted to get the performance parameters, including flow angle δ and mass flow rate m_T of TLF. As shown in Figures 17 and 18, only the m_T and δ of TLF from 15%–25% M increase greatly as the mass flow rate decreases. It indicates that the angle δ and m_T from 15%–25% M have crucial effects on the interaction and blockage. At the large mass flow rates, the angle δ and m_T from 15%–25% M is small. The blockage induced by the interaction is weak. As the mass flow rate decreases, the TLF from 15%–25% M leaves the tip clearance with a larger flow angle δ, and its mass flow rate m_T increases. So the angle between the broken-downed TLV and the TLF from 15%–25% M increases, and the interaction between them is enhanced. The stronger interaction leads to larger blockage, which would induce stronger flow unsteadiness. Particularly, at the mass flow rate of 1.4 kg/s (Figure 19), the TLF from 15%–25% M is almost perpendicular to the streamwise direction, and it is twisted into a new vortex under the influence of broken-downed TLV. The vortex axis is nearly perpendicular to the streamwise direction. The relative velocity vector distribution on plane A, which is almost perpendicular to the vortex axis, shows that, the vortex rotates in anti-clockwise direction, so the relative velocity near the blade tip is opposite to the streamwise direction, and thus the reverse flow is observed. The above flow phenomenon is owing to the "tip separation vortex" as reported by Wu et al. [10]. The interaction between the low-energy leakage fluid from adjacent passages and the broken-downed TLV is responsible for the formation of "tip separation vortex". In this study, the tip separation vortex is formed due to the interactions among separated fluids, broken-downed TLV and TLF from 15%–25% M.

4.2   Possible link to the stall inception

According to ref. [32], because of the blockage induced by TLF from the adjacent blade, the separation is encountered
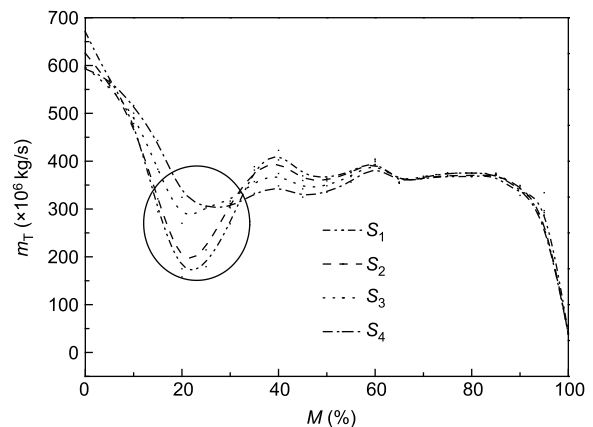

Figure 16 Frequency characteristics of static pressure for different operating points.

Figure 17 Distribution of mass flow rate of TLF along the meridional direction by steady simulation.
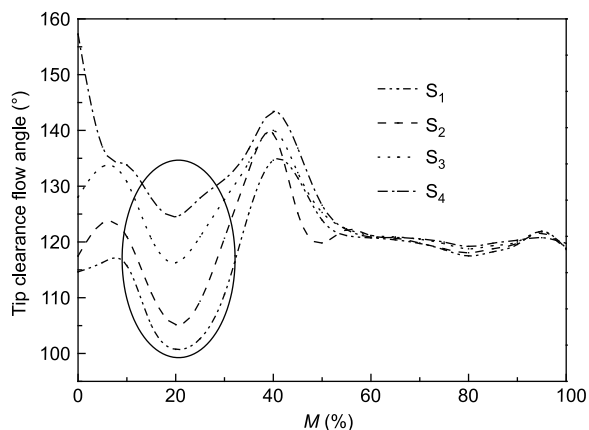
Figure 18   Angle δ distribution along the meridional direction by steady simulation.
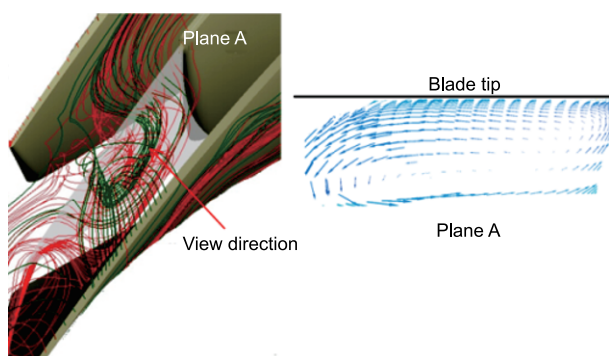

Figure 19   Tip separation vortex at mass flow rate of 1.4 kg/s.

with high incidence, which is responsible for the spike stall. The flow unsteadiness shares the same dynamics with the spike stall, as we proposed in the present study that the blockage induced by the interactions among broken-downed tip leakage vortex, separated fluids and tip leakage flow from 15%–25% M is of vital importance in inducing flow unsteadiness. Immediately before the stall onset, the unsteadiness of this TLF causes multiple transient LE separations that do not persist long enough to propagate in front of the adjacent blades to form a spike. The multiple separations cause multiple disturbances, which are the early signs of a spike stall. In this paper, as shown in Figure 16, at the large mass flow rates, only the main frequency of about 0.5 BPF appears. However, at the mass flow rate of 1.4 kg/s, some lower frequency components emerge, which may be linked to multiple transient LE separations. If the mass flow rate continues to decrease, the LE separations will shed sufficient vorticity to propagate from blade to blade because of the following positive feedback mechanism: the blockage resulted from the flow separation and TLF in one passage increases the incidence on the next blade, causing the next blade to separate, and hence creates a larger blockage in the adjacent passage, and so on.

Thus a rotating stall is formed. This also explains why removing of low speed fluid in the tip region could extend the stability margin. From these results, it is concluded that the TLF unsteadiness may be a factor causing the rotating stall. To identify the lower frequency components, the multi-passage or full passages numerical simulations and experiments on the stall onset process need to be carried out, which is our next work.

5   Conclusions

In this paper, both steady and unsteady numerical simulations are conducted for a centrifugal compressor impeller designed by Krain to investigate the flow unsteadiness in tip region before stall and its unsteady mechanism in a subsonic environment. Some findings are summarized as follows.

(1) The unsteady flow is concentrated in the zone that is influenced by the tip leakage flow (TLF). The oscillating strength on the pressure side is stronger than that on the suction side. The fluctuation frequency of the unsteady flow is a constant, which approximates to 0.477 blade passing frequency (BPF).

(2) Due to the periodical change of blade loading in the tip region, the trajectory and intensity of the tip leakage vortices, and the momentums of TLF as well alter periodically. The interactions among the broken-downed TLV, separated fluids and the TLF from 15%–25% M is responsible for the formation of blockage. The downward movement of blockage leads to a periodic variation of the blade loading near the blade tip. In turn, the blade loading would alter the strength of TLV and TLF, and accordingly the motion of blockage. Such alternative behaviors finally result in a self-sustained unsteady flow oscillation system.

(3) In the model with four passages, the main frequency of flow unsteadiness in four passages are observed to be a constant as 3921 Hz, which is close to the frequency in the model with single passage. The small difference between them may be explained as numerical errors. In addition, the unsteady flow characteristics in the four passages resemble each other, and no phase difference is observed. It is different from the situation when the rotating instability is encountered, in which the unsteady flow propagates against the rotational direction of the impeller.

(4) With the decrease of mass flow rate, the flow unsteadiness becomes more intense, as the flow blockage becomes larger due to the stronger interactions between the broken-downed TLV and TLF. The fluctuation frequency of unsteady flow is also slightly increased. At the near-stall condition, some lower frequency components appear, which may be linked to multiple transient LE separations. When the mass flow rate is small enough, the blockage in one passage will cause the flow separation on the adjacent blade. Thus the flow

separation migrates in front of the adjacent blades, which may trigger a spike stall.

1   Stein A, Niazi S, Sankar L N. Computational analysis of stall and separation control in centrifugal compressors. J Propul Power, 2000, 16: 65–71

2   Hathaway M D, Chriss R M, Wood J R, et al. Experimental and computational investigation of the NASA low-speed centrifugal compressor flow field. J Turbomach, 1993, 115: 527

3   Iwakiri K, Furukawa M, Ibaraki S, et al. Unsteady and three-dimensional flow phenomena in a transonic centrifugal compressor impeller at rotating stall. In: ASME Turbo Expo 2009: Power for Land, Sea, and Air. Orlando: International Gas Turbine Institute, 2009. 1611–1622

4   Tamaki H. Effect of recirculation device with counter swirl vane on performance of high pressure ratio centrifugal compressor. J Turbomach, 2012, 134: 051036

5   Zheng X Q, Lan C J. Effects of blade bowing on the performance of a high pressure-ratio turbocharger centrifugal compressor with self-recirculation casing treatment. Sci China Tech Sci, 2013, 56: 2531–2539

6   Hunziker R, Dickmann H P, Emmrich R. Numerical and experimental investigation of a centrifugal compressor with an inducer casing bleed system. P I Mech Eng A-J Pow, 2001, 215: 783–791

7   Du J, Lin F, Chen J, et al. Flow structures in the tip region for a transonic compressor rotor. J Turbomach, 2013, 135: 031012

8   Du J, Lin F, Zhang H W, et al. Numerical investigation on the self-induced unsteadiness in tip leakage flow for a transonic fan rotor. J Turbomach, 2010, 132: 021017

9   Wu Y H, Li Q P, Tian J T, et al. Investigation of pre-stall behavior in an axial compressor rotor—Part I: Unsteadiness of tip clearance flow. J Turbomach, 2012, 134: 051027

10 Wu Y H, Li Q P, Chu W L, et al. Numerical investigation of the unsteady behaviour of tip clearance flow and its possible link to stall inception. P I Mech Eng A-J Pow, 2010, 224: 85–96

11 Mailach R, Lehmann I, Vogeler K. Rotating instabilities in an axial compressor originating from the fluctuating blade tip vortex. J Turbomach, 2001, 123: 453–463

12 Yang C, Shan S, Li D. Inlet recirculation influence to the flow structure of centrifugal impeller. Chin J Mech Eng, 2010, 23: 647–654

13 Schleer M, Song S J, Abhari R S. Clearance effects on the onset of instability in a centrifugal compressor. J Turbomach, 2008, 130: 031002

14 Bousquet Y, Binder N, Dufour G, et al. Numerical investigation of Kelvin-Helmholtz instability in a centrifugal compressor operating near stall. J Turbomach, 2016, 138: 071007

15 Hoying D A, Tan C S, Vo H D, et al. Role of blade passage flow structurs in axial compressor rotating stall inception. J Turbomach, 1999, 121: 735–742

16 Vo H D, Tan C S, Greitzer E M. Criteria for spike initiated rotating stall. J Turbomach, 2008, 130: 011023

17 Chen J P, Hathaway M D, Herrick G P. Prestall behavior of a transonic axial compressor stage via time-accurate numerical simulation. J Turbomach, 2008, 130: 041014

18 Tong Z T, Lin F, Chen J. Y, et al. The self-induced unsteadiness of tip leakage vortex and its effect on compressor stall inception. In: ASME Turbo Expo 2007: Power for Land, Sea, and Air. Montreal: International Gas Turbine Institute, 2007. 1551–1562

19 Krain H, Hoffmann B, Pak H. Aerodynamics of a centrifugal compressor impeller with transonic inlet conditions. In: ASME 1995 International Gas Turbine and Aeroengine Congress and Exposition. Houston: International Gas Turbine Institute, 1995

20 Eisenlohr G, Krain H, Richter F A, et al. Investigations of the flow through a high pressure ratio centrifugal impeller. In: ASME Turbo Expo 2002: Power for Land, Sea, and Air. Amsterdam: International Gas Turbine Institute, 2002. 649–657

21 Kaneko M, Tsujita H. Numerical investigation of influence of tip leakage flow on secondary flow in transonic centrifugal compressor at design condition. J Therm Sci, 2015, 24: 117–122

22 Decaix J, Balarac G, Dreyer M, et al. RANS and LES computations of the tip-leakage vortex for different gap widths. J Turbulence, 2015, 16: 309–341

23 Roberts D A, Steed R. A comparison of steady-state centrifugal stage CFD analysis to experimental rig data. In: Proceedings of the ANSYS User's Conference, 2004. 10–13

24 Zhao H J, Wang Z H, Yu H S, et al. Numerical investigation of the shock effects on the performance and flow field in transonic centrifugal impeller. In: ASME Turbo Expo 2016: Turbomachinery Technical Conference and Exposition, 2016

25 Bae J, Breuer K S. Periodic unsteadiness of compressor tip clearance vortex. In: ASME Turbo Expo 2004: Power for Land, Sea, and Air. Vienna: International Gas Turbine Institute, 2004. 457–465

26 Degani D, Levy Y, Seginer A. Graphical visualization of vortical flows by means of helicity. AIAA J, 1990, 28: 1347–1352

27 Chen G T, Greitzer E M, Tan C S, et al. Similarity analysis of compressor tip clearance flow structure. J Turbomach, 1991, 113: 260–269

28 Kang S, Hirsch C. Numerical simulation of three-dimensional viscous flow in a linear compressor cascade with tip clearance. J Turbomach, 1996, 118: 492–505

29 Liu Z X, Ping Y, Zangeneh M. On the nature of tip clearance flow in subsonic centrifugal impellers. Sci China Tech Sci, 2013, 56: 2170–2177

30 März J, Hah C, Neise W. An experimental and numerical investigation into the mechanisms of rotating instability. J Turbomach, 2002, 124: 367–375

31 Krain H, Hoffmann B, Rohne K H, et al. Improved high pressure ratio centrifugal compressor. In: ASME Turbo Expo 2007: Power for Land, Sea, and Air. Montreal: International Gas Turbine Institute, 2007. 967–975

32 Pullan G, Young A M, Day I J, et al. Origins and structure of spike-type rotating stall. J Turbomach, 2015, 137: 051007